

See discussions, stats, and author profiles for this publication at: <https://www.researchgate.net/publication/229811196>

# On the Physico-Chemical Properties of ZnO Nanosheets Modified with Luminescent CdTe Nanocrystals

ARTICLE in THE JOURNAL OF PHYSICAL CHEMISTRY C · DECEMBER 2011

Impact Factor: 4.77 · DOI: 10.1021/jp209267s

CITATIONS

13

READS

32

5 AUTHORS, INCLUDING:



**Daniele Costenaro**

Amedeo Avogadro University of Eastern Pied...

11 PUBLICATIONS 79 CITATIONS

SEE PROFILE



**Fabio Carniato**

Amedeo Avogadro University of Eastern Pied...

79 PUBLICATIONS 901 CITATIONS

SEE PROFILE



**Giorgio Gatti**

Amedeo Avogadro University of Eastern Pied...

54 PUBLICATIONS 556 CITATIONS

SEE PROFILE



**Leonardo Marchese**

Amedeo Avogadro University of Eastern Pied...

255 PUBLICATIONS 5,702 CITATIONS

SEE PROFILE

# On the Physico-Chemical Properties of ZnO Nanosheets Modified with Luminescent CdTe Nanocrystals

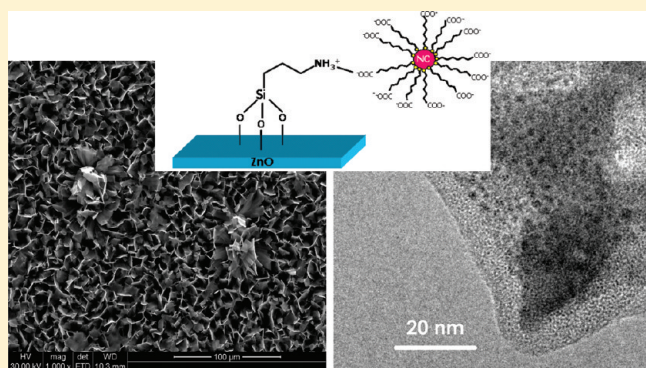
Daniele Costenaro,<sup>†</sup> Fabio Carniato,<sup>†</sup> Giorgio Gatti,<sup>†</sup> Chiara Bisio,<sup>\*,†,‡</sup> and Leonardo Marchese<sup>†</sup>

<sup>†</sup>Dipartimento di Scienze e Tecnologie Avanzate and Nano-SISTEMI Interdisciplinary Centre, Università del Piemonte Orientale “A. Avogadro”, via Teresa Michel 11, I-15121 Alessandria, Italy

<sup>‡</sup>ISTM-CRN Istituto di Scienze e Tecnologie Molecolari, via G. Venezian 21, Milano, Italy

 Supporting Information

**ABSTRACT:** ZnO nanosheets were synthesized through thermal decomposition of the  $\text{Zn}_4\text{CO}_3(\text{OH})_6 \cdot \text{H}_2\text{O}$  precursor at increasing temperatures (i.e., 300, 400, and 500 °C), and a multidisciplinary characterization (carried out by X-ray diffraction, SEM and TEM microscopy, FTIR, diffuse reflectance UV–vis and photoluminescence spectroscopy, TGA, and nitrogen adsorption) allowed us to describe the dependence of the physicochemical properties of the final materials on the precursor decomposition temperature. Due to its interesting physicochemical properties (good electrical conductivity, adequate specific surface area, and significant concentration of surface OH groups suitable for silylation reactions), the ZnO sample, prepared by thermal decomposition of  $\text{Zn}_4\text{CO}_3(\text{OH})_6 \cdot \text{H}_2\text{O}$  at 400 °C (named ZnO400), was selected as the host solid for the introduction of guest luminescent CdTe nanocrystals. The modification of the ZnO surface with CdTe allowed us to change the optical properties of the final solid, resulting in a tuning of emission properties of the ZnO nanosheets.



## INTRODUCTION

In the last years, inorganic nanostructured materials (spanning from silica nanoparticles to layered materials, mesoporous solids, and metal oxides) have stimulated great interest due to their importance in basic scientific research and their potential technological applications.

In this context, zinc oxide (ZnO) derivatives showed interesting potentialities in several technological applications.<sup>1–7</sup> ZnO is a wide bandgap (3.37 eV) semiconductor having a high electron–hole binding energy (60 meV), which finds several important applications in electronics, optoelectronics (i.e., light-emitting diodes), and laser production.<sup>8</sup> In addition, piezoelectric and pyroelectric properties make ZnO a good candidate for the optimization of sensors, transducers, energy generators, and photocatalysts for hydrogen production. ZnO is also considered a “green” material because it is biocompatible, biodegradable, and biosafe, thus extending its applications to medical and environmental science.<sup>9–12</sup>

For all these reasons, the number of papers related to ZnO nanostructures exponentially increased in the last years: considering the 2010 year, for instance, over 800 articles concerning this semiconductor have been published.

Because of their potential applications, micro- and nanostructured ZnO materials with various particle sizes and morphologies, such as nanowires,<sup>13</sup> nanorods,<sup>14</sup> nanobelts/ribbons,<sup>15</sup> nanosheets, nanodiscs,<sup>16</sup> and nanoflowers,<sup>17</sup> have been prepared

and optimized by using different synthetic approaches. Among these, solution methods have attracted increased interest and have been employed to grow nano- and microstructured ZnO matrices.<sup>18</sup> In particular, electrodeposition,<sup>19,20</sup> hydrothermal processes,<sup>21,22</sup> reverse microemulsion,<sup>23</sup> thermal oxidation in water vapor,<sup>24</sup> and chemical bath deposition (CBD)<sup>25–27</sup> have been largely adopted. This last technique is especially used because it requires a simple approach and easily allows us to obtain ZnO solids with controlled morphology. This technique is also suitable for the production of ZnO thin films<sup>25</sup> of large interest for nanotechnological purposes.

Very recently, ZnO-based materials have attracted particular interest for the preparation of blue and ultraviolet (UV) laser devices because of their wide band gap and large exciton binding energy. ZnO usually exhibits both a near-band-edge emission ( $\lambda_{\text{em}} = 380 \text{ nm}$ ) and a visible ( $\lambda_{\text{em}} = 500–600 \text{ nm}$ ) luminescence band, which are significantly dependent on the growth methods and on the preparation conditions.<sup>28</sup> The UV near-band-edge luminescence in ZnO powders is generally quenched, and the broad visible emission, due to solid defects, is usually predominant. This is especially evident for defective ZnO nanoparticles,

**Received:** September 26, 2011

**Revised:** November 16, 2011

**Published:** November 18, 2011

while micrometric ZnO particles show reduced visible photo-emission.

Great efforts have been done to improve and/or modify the emission properties of ZnO semiconductors aiming to adapt their optical properties to the required specifications. For instance, it was found that the capping procedure of ZnO particles with different light-emitting entities, such as polymer, alkali halide crystal, organic dye, etc., can effectively modify the photoluminescence properties of the final hybrid solids.<sup>29</sup> These modifications are usually made by postsynthesis approaches and lead to the formation of weak interactions among the two phases. For example, the addition of quantum dot nanocrystals (i.e., CdSe and CdTe) on the ZnO surface is generally done by promoting electrostatic interactions between the solids, and it resulted in a significant modification of ZnO emission properties.<sup>30</sup>

In this paper, ZnO with nanosheet-like morphology derived from a zinc carbonate hydroxide hydrate ( $\text{Zn}_4\text{CO}_3(\text{OH})_6 \cdot \text{H}_2\text{O}$ ) precursor has been synthesized adapting a methodology reported in the literature.<sup>31</sup> Particular emphasis was devoted to the investigation of the physicochemical properties of ZnO materials prepared by decomposition of the precursor at temperature in the 300–500 °C range. Combined XRD, SEM, HR-TEM,  $\text{N}_2$  physisorption, and FTIR analyses allowed us to obtain information on the crystallinity, morphology, and textural and surface properties of the prepared materials. On the basis of the collected data, augmented by the analysis of the electrical behavior of produced solids, the definition of the optimal procedure for the production of nanostructured ZnO suitable for postsynthesis modification with luminescent entities was carried out.

The most suitable solid in terms of surface hydroxyl group populations (needed for chemical anchoring of organic species), high specific surface area (suitable to increase the amount of functional groups), and conduction behavior was then modified with CdTe nanocrystals, and the physicochemical properties of the novel CdTe/ZnO composite solid were studied, with special attention to its optical properties.

## EXPERIMENTAL SECTION

**Materials Preparation.** *ZnO Nanosheet.* ZnO with nanosheet morphology was prepared by thermal decomposition of the  $\text{Zn}_4\text{CO}_3(\text{OH})_6 \cdot \text{H}_2\text{O}$  precursor obtained by chemical bath deposition (CBD), adapting a methodology reported in the literature:<sup>31</sup> 0.55 g of hydrated zinc acetate ( $\text{Zn}(\text{CH}_3\text{COO})_2 \cdot 2\text{H}_2\text{O}$ , Sigma Aldrich) was added to 3.00 g of urea (Sigma Aldrich) in 50 mL of deionized water, and the pH value of the solution was adjusted to 4.5 by using acetic acid. The solution was then transferred in an autoclave, in the presence of a commercial borosilicate glass slide (previously washed in a Piranha solution made of  $\text{H}_2\text{SO}_4$  and  $\text{H}_2\text{O}_2$  in 3:1 volume ratio), and kept at 80 °C for 12 h. After this time, a film of  $\text{Zn}_4\text{CO}_3(\text{OH})_6 \cdot \text{H}_2\text{O}$  precursor was formed on the glass slide surface. In parallel,  $\text{Zn}_4\text{CO}_3(\text{OH})_6 \cdot \text{H}_2\text{O}$  in powder form was also recovered. Both powder and film were finally heated in air to promote the decomposition of  $\text{Zn}_4\text{CO}_3(\text{OH})_6 \cdot \text{H}_2\text{O}$  with the consequent formation of ZnO solid. Three different calcination temperatures at 300, 400, and 500 °C were explored, allowing the preparation of three different ZnO samples, named ZnO300, ZnO400, and ZnO500, respectively.

*ZnO Functionalized with Amino Groups.* An amount of 0.500 g of the ZnO400 sample in powder form was treated in vacuum ( $1.5 \times 10^{-3}$  mbar residual pressure) at 200 °C for 15 h, to

remove physisorbed water. After treatment, the sample was dispersed in an ethanol/water mixture (95%/5% V/V). The pH value of the solution was adjusted to 5 by dropping acetic acid. The suspension was sonicated for 20 min, after addition of 1.3 mL of 3-aminopropyltriethoxysilane (Sigma Aldrich), APS, and transferred in an oven at 75 °C for 1 h. The suspension was finally filtered and the powder washed with ethanol and ethyl ether to remove the unreacted silane. The obtained sample was named APS/ZnO400.

*ZnO Functionalized with CdTe Nanoparticles.* CdTe nanocrystals of ca. 3.4 nm in diameter, capped with thioglycolic acid (kindly supplied by the research group of Prof. A. Eychmueller, Technische Universität Dresden), were bound to the APS/ZnO400 surface by using the following procedure: 1.0 g of APS/ZnO400 was dispersed in 40 mL of deionized water and sonicated for 15 min. An amount of 30 mL of a CdTe suspension ( $1 \times 10^{-5}$  M) was added to the APS/ZnO400 dispersion (pH = 7.0), and the mixture was stirred for 20 h at room temperature. Then, the powder was filtered and washed with deionized water to remove the unreacted CdTe nanocrystals. The obtained sample was named CdTe/ZnO400.

### Characterization Techniques

- The chemical composition of CdTe/ZnO400 was determined with inductively coupled plasma-mass spectrometry (ICP-MS) by ITECON srl laboratory [Nizza Monferrato (AT), Italy].
- X-ray diffraction (XRD) patterns were obtained on an ARL XTRA48 diffractometer using  $\text{Cu K}\alpha$  radiation ( $\lambda = 1.54062$  Å). A variable-temperature X-ray diffraction (VT-XRD) profile was also measured from rt to 500 °C under air flow (100 mL/min) by using a Buelher high-temperature stage. The sample deposited on a Pt/Rh strip was heated at 5 °C  $\text{min}^{-1}$  and left to equilibrate at each temperature for 10 min, before the diffractogram was registered.
- Scanning electron microscopy (SEM) analyses were performed using a LEO 1450 VP instrument, coating the samples with a thin gold layer to ensure surface conductivity.
- TEM images were collected on a JEOL 3010 High Resolution Transmission Electron Microscope operating at 300 kV. Specimens were prepared by sonicating the sample in isopropanol and by depositing a few drops of the suspension on carbon-coated grids. The microscope was equipped with an Oxford Instruments INCA TEM 200 system for energy-dispersive X-ray spectroscopy (EDS) analysis.
- $\text{N}_2$  physisorption measurements were carried out at 77 K in the relative pressure range from  $1 \times 10^{-5}$  to  $1 P/P_0$  by using a Quantachrome Autosorb 1MP/TCD instrument. Prior to the analysis the samples were outgassed (residual pressure lower than  $10^{-6}$  mbar) at 150 °C for 15 h. Upon this treatment, only water is removed from the samples. Apparent surface areas were determined by using the Brunauer–Emmett–Teller equation, in the relative pressure range from 0.01 to  $0.1 P/P_0$ . Pore size distributions were obtained by applying the NLDFT method ( $\text{N}_2$  silica kernel based on a cylindrical pore model applied to the desorption branch).
- TGA analyses were performed on a Setaram SETSYS Evolution instrument under oxygen (gas flow 20 mL/min), heating the samples up to 800 °C with a rate of 10 °C/min.
- IR spectra were collected on a Bruker Equinox 55 (resolution of 4  $\text{cm}^{-1}$ ) equipped with pyroelectric DTGS



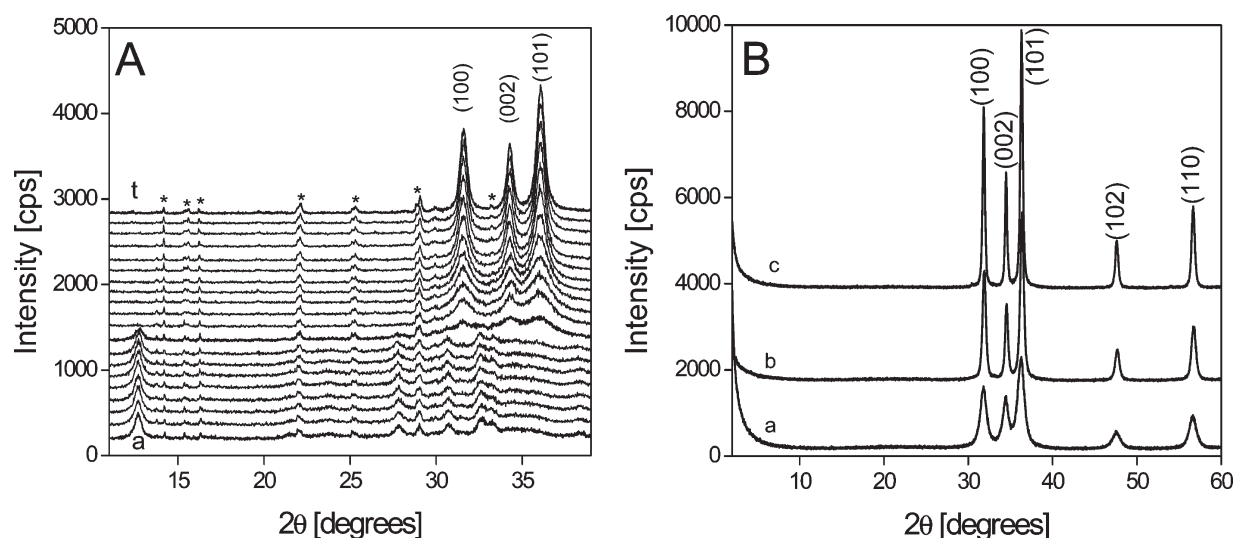


**Figure 1.** (A) XRD patterns at variable temperature of  $\text{Zn}_4\text{CO}_3(\text{OH})_6 \cdot \text{H}_2\text{O}$ : (a) rt, (b) 50 °C, (c) 75 °C, (d) 100 °C, (e) 125 °C, (f) 150 °C, (g) 175 °C, (h) 200 °C, (i) 225 °C, (j) 250 °C, (k) 275 °C, (l) 300 °C, (m) 325 °C, (n) 350 °C, (o) 375 °C, (p) 400 °C, (q) 425 °C, (r) 450 °C, (s) 475 °C, (t) 500 °C; reflections with an asterisk are due to contamination products stably bound to the Pt/Rh sample holder. (B) XRD profiles of ZnO prepared by treatment of  $\text{Zn}_4\text{CO}_3(\text{OH})_6 \cdot \text{H}_2\text{O}$  at 300 °C (a), 400 °C (b), and 500 °C (c).

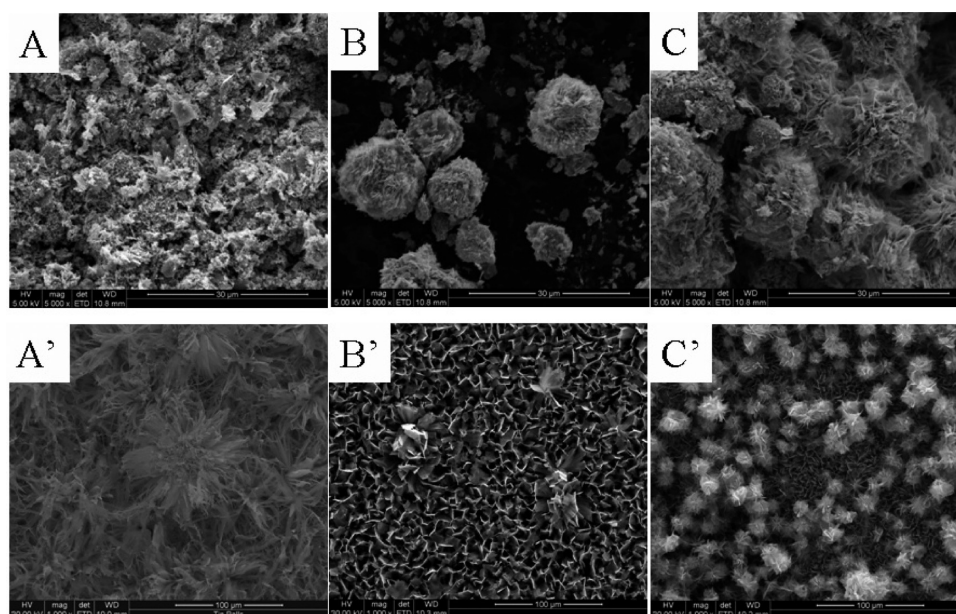


**Figure 2.** SEM images of the ZnO300, ZnO400, and ZnO500 in powder (A, B, and C, respectively) and film form (A', B', and C', respectively).

(KBr cells, path length 0.5 mm). The samples in the form of pellets were placed into a IR cell equipped with KBr windows permanently attached to a high vacuum line (residual pressure:  $1.0 \times 10^{-6}$  mbar, 1 mbar = 10 Pa). The samples were measured both in air and under vacuum at room temperature.

- Diffuse reflectance UV–visible (DR–UV–vis) spectra were recorded using a Perkin-Elmer Lambda 900 spectrometer equipped with a diffuse reflectance sphere accessory. Prior to the analysis, the samples were dispersed in anhydrous  $\text{BaSO}_4$  (5 wt %).
- Photoemission spectra were acquired with a Horiba Jobin Yvon Fluorolog TCSPC spectrofluorimeter equipped with a 450 W xenon lamp and a Hamamatsu R928 photomultiplier.

- $I$ – $V$  curves of ZnO300, ZnO400, and ZnO500 films were collected with the instrument model 2400 General-Purpose SourceMeter of Keithley Company.

## RESULTS AND DISCUSSION

**Physico-Chemical Characterization of ZnO Nanosheets.** The structural modifications of  $\text{Zn}_4\text{CO}_3(\text{OH})_6 \cdot \text{H}_2\text{O}$  powder were followed by variable-temperature X-ray diffraction (VT-XRD). The X-ray profile of the sample collected at room temperature (Figure 1A, curve a) showed peaks in the range 10–40°  $2\theta$  typical of the  $\text{Zn}_4\text{CO}_3(\text{OH})_6 \cdot \text{H}_2\text{O}$  phase,<sup>31</sup> thus indicating that the adopted synthesis allowed us to prepare the desired ZnO precursor.

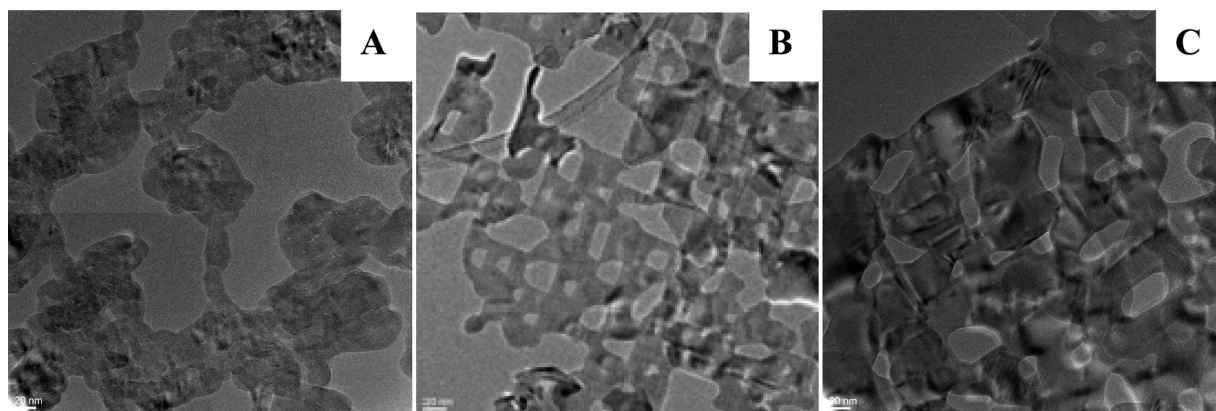


Figure 3. TEM micrographs of ZnO300 (A), ZnO400 (B), and ZnO500 (C) samples.

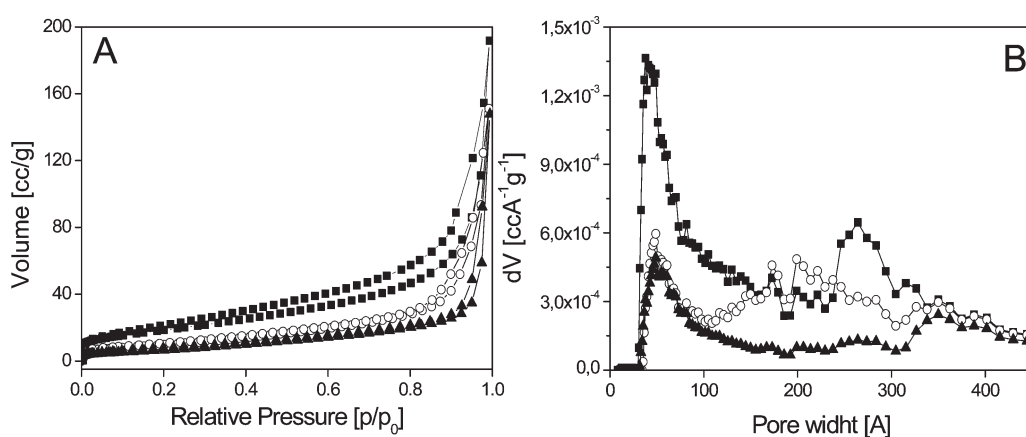


Figure 4. N<sub>2</sub> adsorption/desorption isotherms at  $-196\text{ }^{\circ}\text{C}$  (A) and pore size distribution (B) of ZnO300 ( $\blacksquare$ ), ZnO400 ( $\circ$ ), and ZnO500 ( $\blacktriangle$ ) samples.

As derived from Figure 1A, the  $\text{Zn}_4\text{CO}_3(\text{OH})_6\cdot\text{H}_2\text{O}$  structure was not modified by heating up to  $200\text{ }^{\circ}\text{C}$  (Figure 1A, curves a–h). By contrast, the X-ray profile measured at  $225\text{ }^{\circ}\text{C}$  (Figure 1A, curve i) drastically changed: the  $\text{Zn}_4\text{CO}_3(\text{OH})_6\cdot\text{H}_2\text{O}$  reflections became weak and broad, and three new peaks at  $31.9$ ,  $34.5$ , and  $36.3^{\circ} 2\theta$ , respectively, due to the (100), (002), and (101) planes of the ZnO phase, appeared. This suggested that the precursor began to be transformed into ZnO at  $225\text{ }^{\circ}\text{C}$ , as already reported in the literature.<sup>31</sup> The treatment at higher temperatures (from  $300$  to  $500\text{ }^{\circ}\text{C}$ ) resulted in an increase of ZnO crystallinity, as indicated by the progressive increase of the intensity and sharpness of the ZnO diffraction peaks (Figure 1A, curves l–t).

On the basis of the variable-temperature XRD results reported in Figure 1A, three different decomposition temperatures (i.e.,  $300$ ,  $400$ , and  $500\text{ }^{\circ}\text{C}$ ) for the precursor were selected to prepare ZnO samples (ZnO300, ZnO400, and ZnO500) with different morphology and surface properties. The diffractograms of these materials are reported in Figure 1B. As expected, the calcination temperature significantly influenced the crystallinity of the ZnO product. Indeed, the intensity and sharpness of the peaks due to the (100), (002), (101), (102), and (110) planes of the ZnO significantly increased passing from ZnO300 (Figure 1B, curve a) to ZnO500 (Figure 1B, curve c). XRD data collected for ZnO films showed peaks typical of ZnO phases (Figure S1 of Supporting Information, SI). Nevertheless, the relative intensity of reflections due to the ZnO phase (i.e., (100), (002), and (101) planes)

is different with respect to samples in powder form (treated in the same conditions) due to preferential orientations induced by film growth on solid support.

The morphology of the ZnO solids in both powder and film form was investigated by scanning electron microscopy (SEM).

ZnO300 in powder form was characterized by crystals with layered morphology organized in irregular aggregates (Figure 2A), similar to those observed for the  $\text{Zn}_4\text{CO}_3(\text{OH})_6\cdot\text{H}_2\text{O}$  precursor (Figure S2 of SI). Particles with layered morphology were also observed for ZnO400 (Figure 2B) and ZnO500 (Figure 2C) samples. However, the crystal organization of these solids significantly changed in comparison to the ZnO300 sample. A partial organization of the crystals in aggregates with rosette-like shape, along with a significant reduction of the lamellae size, was observed for the ZnO400 sample (Figure 2B). This aggregation phenomenon was more evident for the ZnO500 sample (Figure 2C), where a large number of rounded-shape aggregates were observed. SEM results suggested that the calcination temperature strongly affected morphology and size of the produced particles.

The morphology of samples in film form was also investigated to estimate the effect of the support on the ZnO crystals organization and growth. For all samples, the formation of homogeneous films was observed. The crystals with layered morphology in ZnO300 film (Figure 2A') appeared slightly organized on the solid support. The calcination temperature strongly affected the

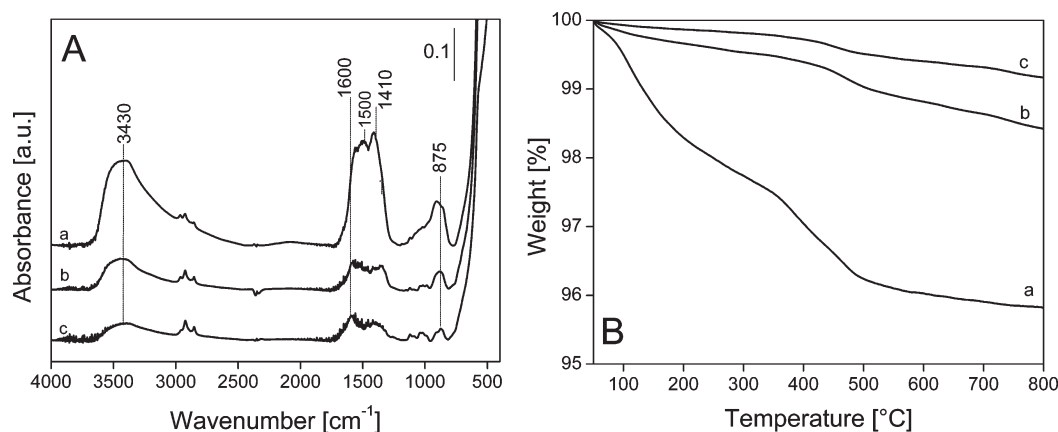


**Figure 5.** (A) IR spectra of ZnO300 (a), ZnO400 (b), and ZnO500 (c) diluted in the KBr matrix (ca. 20 wt %), collected in vacuum at room temperature. (B) TGA analyses of ZnO300 (a), ZnO400 (b), and ZnO500 (c) recorded under O<sub>2</sub> flow (100 mL/min).

organization of ZnO crystals on the glass slide. Indeed, ZnO400 and ZnO500 samples presented a homogeneous layer of crystals with regular shape perpendicularly oriented with respect to the support (Figure 2B' and C', respectively). In addition, aggregates with rosette-like shape, already observed in ZnO400 and ZnO500 powder samples, covered part of the ZnO layer formed on the glass slide. These aggregates were especially observed for the ZnO500 sample (Figure 2C').

Representative TEM images of ZnO nanosheets are shown in Figure 3. All samples exhibited a macroporous structure, whose pore dimensions are dependent on the calcination temperature. This porous structure resulted from the interconnection of ZnO grains and is typical of solids prepared at relatively low temperature (below 500 °C).<sup>31</sup> According to the literature, the evolution of such a nanosheet structure is one peculiar feature of the fabrication method here proposed, which is different from other chemical solution based methods where single crystalline or dense ZnO phases are commonly obtained.

The effect of the calcination temperature on the textural features of the ZnO materials, in terms of specific surface area and pore size distribution, was also investigated by carrying out N<sub>2</sub> physisorption experiments on samples in powder form (Figure 4).

Figure 4A shows the nitrogen adsorption–desorption isotherm plots of the ZnO samples, which correspond to the so-called “type III” isotherm in the Brunauer classification. A hysteresis loop “H3” was observed for ZnO300 and ZnO400 samples and can be associated to the presence of slit-shaped pores, relative to the formation of interspaces between the nanosheets, according to TEM analysis. ZnO500 did not show a hysteresis loop, indicating a reduced porosity for this sample. The specific surface area, estimated by the BET algorithm, decreased with the calcination temperature, passing from 68 for ZnO300 to 37 and 25 m<sup>2</sup>/g for ZnO400 and ZnO500, respectively.

This is in agreement with the IR data that showed a progressive decrease of the band intensity of OH groups exposed on the ZnO surface as a function of the treatment temperature (*vide infra*).

The porosity was estimated by the NLDFT method. ZnO300 showed a bimodal pore diameter distribution, with maxima centered at 50 and 280 Å, due to aggregation of the nanosheets (Figure 4B). The average pore volume calculated for the ZnO300 sample was 0.21 cc/g.

A different pore diameter distribution was observed for ZnO400 and ZnO500 samples in comparison to ZnO300 solid.

In particular, the mesopores observed for the ZnO300 sample in the range 200–300 Å gradually decreased by increasing the calcination temperature, and the pore volume passed from 0.21 cc/g for the ZnO300 sample to 0.17 and 0.12 cc/g for the ZnO400 and ZnO500 samples, respectively, thus confirming a progressive reduction of the intraparticle porosities.

ZnO samples in powder form were characterized by infrared spectroscopy aiming to evaluate the effects of the calcination temperature on the final surface properties of the samples. IR spectra of all solids after treatment in vacuum at room temperature are reported in Figure 5.

The IR spectrum of ZnO300 (Figure 5A, a) showed a broad band in the 3600–3200 cm<sup>-1</sup> range with a maximum centered at 3430 cm<sup>-1</sup>, which can be assigned to the stretching mode of OH groups of adsorbed water (the bending mode falling at 1600 cm<sup>-1</sup>) and OH groups of residual hydroxycarbonate species. The stretching vibration of OH groups on the ZnO surface should absorb in the 3600–3200 cm<sup>-1</sup> range and cannot be distinguished by the band of adsorbed water. Three additional peaks at 1500, 1410, and 875 cm<sup>-1</sup> (with a weak shoulder at higher frequencies) were also observed in the ZnO300 spectrum and assigned to the asymmetric stretching modes (bands at 1500 and 1410 cm<sup>-1</sup>) and out-of-phase bending mode (peak at 875 cm<sup>-1</sup>) of COO<sup>-</sup> species of residual hydroxycarbonates still present on the sample after the calcination of the Zn<sub>4</sub>CO<sub>3</sub>(OH)<sub>6</sub>·H<sub>2</sub>O precursor.

The surface properties of ZnO obtained by calcination at higher temperatures appeared modified in comparison to those of ZnO300 (Figure 5A, curves b and c). Indeed, the bands due to stretching of OH groups at 3430 and 1600 cm<sup>-1</sup> along with those typical of hydroxycarbonate species (at 1500, 1410, and 875 cm<sup>-1</sup>) appeared decreased in intensity for both samples. This was particularly evident in the case of the ZnO500 sample (Figure 5A, c). This behavior indicated a progressive reduction of adsorbed water and residual hydroxycarbonates exposed on the ZnO surface by increasing the calcination temperature. The amount of precursor species in the final ZnO solids was estimated by thermogravimetric analysis collected under oxygen flow, from 50 to 800 °C (Figure 5B).

The thermal profile of the ZnO300 sample (Figure 5B, a) showed three weight losses, the first one below 100 °C due to the removal of adsorbed water, the second one of ca. 2.3 wt % in the range 100–350 °C ascribed to the decomposition of residual



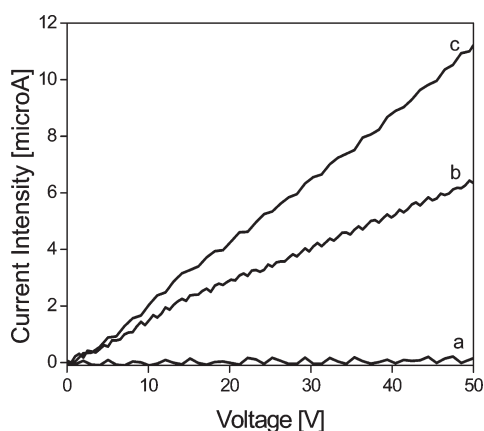


**Figure 6.**  $I$ – $V$  curves of ZnO300 (a), ZnO400 (b), and ZnO500 (c) films.

hydroxycarbonates, and the last at temperature higher than 350 °C probably due to the removal of carbonates remaining at the surface of the ZnO sample (Figure 5A). Similar profiles were observed for ZnO400 and ZnO500 samples (Figure 5B, b and c, respectively). Nevertheless, for these samples the amount of carbonate species was ca. 1 wt % and 0.5 wt %, respectively, confirming that the ZnO prepared at higher temperatures contained a limited amount of residual hydroxycarbonates and carbonates, in agreement with the spectroscopic data.

The conductivity properties of ZnO prepared with different calcination temperatures were also explored. The  $I/V$  curves collected for ZnO samples prepared in the film form are reported in Figure 6. The current intensity for the ZnO300 sample, measured from 0 to 50 V, was constant and close to zero, suggesting that this sample had an insulating character (Figure 6, curve a). By contrast, ZnO400 and ZnO500 films showed a linear  $I/V$  curve with positive slope (Figure 6, curves b and c) typical of semi-conductive materials.

The resistance and resistivity of the ZnO samples can be derived by the  $I/V$  curves above-described, by using the following equations

$$V = R \cdot I \quad (1)$$

where  $R$  (resistance) can be derived by the slope of the  $I/V$  curves

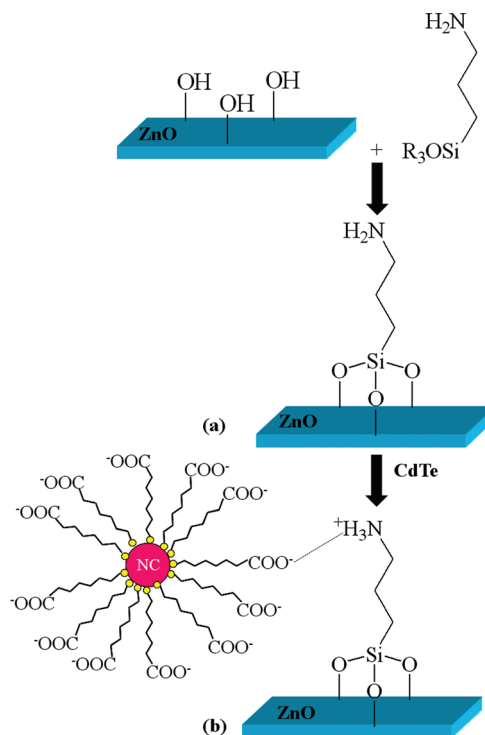
$$R = \rho \cdot \frac{l}{S} \quad (2)$$

$l = 6$  mm is the distance of the two electrodes used to measure the  $I/V$  curves;  $S = 10$  mm<sup>2</sup> is the material surface studied; and  $\rho$  is the resistivity.

The resistivity values decreased, passing from  $8.61 \times 10^8$  for ZnO300 to  $1.38 \times 10^7$  for ZnO400 and  $9.61 \times 10^6$  for ZnO500, thus suggesting that the electrical conductivity increased with the calcination temperature used to prepare the ZnO solids. This can be strictly correlated to the crystallinity and homogeneity of the ZnO films that significantly increased passing from ZnO300 to ZnO500 sample, as derived from XRD and SEM studies.

**Luminescent Organo-Modified ZnO Nanosheets.** Due to its interesting physicochemical properties in terms of electrical conductivity, morphology, and surface features, the ZnO400 sample was functionalized with amino groups, through anchoring of aminopropyltriethoxysilane at pH = 5 on the OH groups

**Scheme 1.** Schematic Representation of the Synthesis Pathways of APS/ZnO400 (a) and CdTe/ZnO400 Samples (b)



exposed on the ZnO surface (Scheme 1). This synthesis strategy was adopted to allow the introduction of species able to bind by ionic interactions CdTe nanocrystals (NCs, dimension of ca. 3.4 nm) capped with thioglycolic acid bearing negatively charged carboxylate groups (see Scheme 1). The synthesis was carried out in water suspension at pH 7 to ensure the deprotonation of  $-\text{COO}^-$  present on the surface of CdTe and the protonation of the  $-\text{NH}_3^+$  units on the ZnO support.

The Cd amount in the CdTe/ZnO400 sample, quantified by elemental analysis (ICP/MS), was  $62.6 \pm 9.0$  mg/g, corresponding to a Cd/Zn ratio of 6 wt %.

The distribution of CdTe nanocrystals on the surface of ZnO nanoparticles was estimated by TEM microscopy (Figure 7, A and B). In addition, TEM micrographs of pure CdTe nanocrystals were collected to estimate their morphology and particle size, aiming to have a reference for TEM images of the CdTe/ZnO400 sample (see Figure S3 in the SI). The contrast and the size of the nanoparticles in the hybrid material perfectly match those of the pure CdTe used as a reference, thus we can safely conclude that CdTe nanocrystals are well dispersed on the surface of ZnO (black spots in Figure 7).

The organic species on the surface of the APS/ZnO400 sample and their interactions with CdTe nanocrystals were monitored by IR spectroscopy (Figure 8A).

Beside the bands typical of ZnO400, the IR spectrum of the APS/ZnO400 sample showed additional absorptions at 3250 and 3130  $\text{cm}^{-1}$  assigned to the asymmetric and symmetric vibrational modes of the protonated amino groups, respectively, and bands at 2930 and 2850  $\text{cm}^{-1}$  due to the asymmetric and symmetric stretching modes of  $-\text{CH}_2$  groups of the propyl chain introduced on the ZnO surface (Figure 8A, b). In addition, the

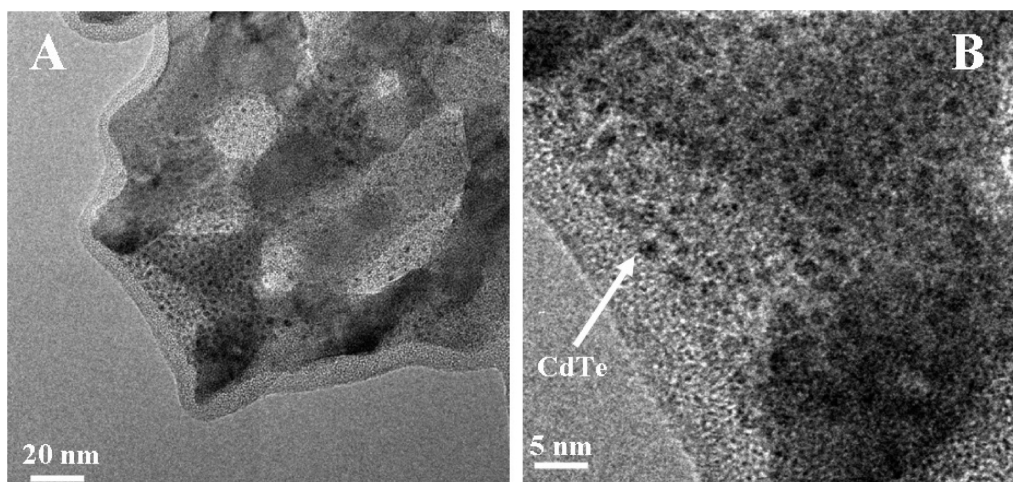


Figure 7. TEM micrographs of the CdTe/ZnO400 sample at low (A) and high (B) magnifications.

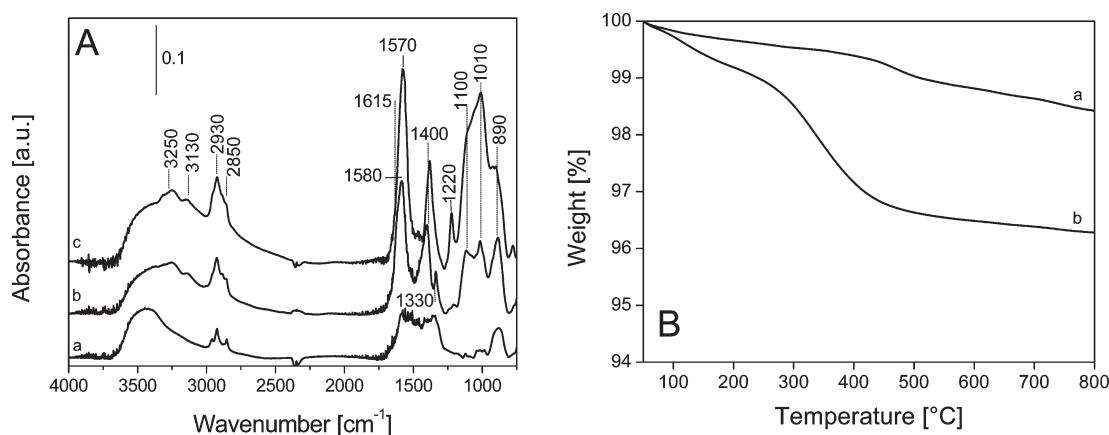


Figure 8. (A) IR spectra of ZnO400 (a), APS/ZnO400 (b), and CdTe/ZnO400 (c) samples diluted in KBr matrix (10 wt %) and collected in vacuum at room temperature. (B) TG analysis collected under  $O_2$  flow (100 mL/min) of ZnO400 (a) and APS/ZnO400 (b) samples.

wide band in the range  $3600\text{--}3200\text{ cm}^{-1}$ , mainly due to stretching of surface OH groups of the ZnO400 sample, decreased in intensity after reaction with aminopropyltriethoxysilane, thus suggesting that a significant fraction of OH groups of the support was involved in the reaction with the organosilane. Vibrational modes of the aminopropyl species were observed at 1615, 1580, 1400, and  $1330\text{ cm}^{-1}$  (Figure 8A, b). The first two bands were assigned to asymmetric and symmetric bending modes of ammonium species ( $-\text{NH}_3^+$ ), respectively, while the absorptions at 1400 and  $1330\text{ cm}^{-1}$  were assigned to the bending and wagging of methylene units, respectively. Bands at 1100 and  $890\text{ cm}^{-1}$  can be attributed to the asymmetric and symmetric stretching of Si—O—Si groups, respectively, deriving by a partial condensation of the organosilanes used to modify the ZnO400 surface. The peak centered at  $1010\text{ cm}^{-1}$  was clear evidence of the formation of the Zn—O—Si bond.<sup>32</sup>

The IR spectrum of CdTe/ZnO400 (Figure 8A, curve c) showed significant differences with respect to that of the APS/ZnO400 sample, mainly in the low wavenumber region. In particular, a band at  $1570\text{ cm}^{-1}$ , strongly overlapped to the bending modes of the  $-\text{NH}_3^+$  group at  $1615\text{--}1580\text{ cm}^{-1}$ , is formed. This band, which is due to the asymmetric stretching modes of  $-\text{COO}^-$  species bound to CdTe nanocrystals (the symmetric

stretching mode falling at ca.  $1400\text{ cm}^{-1}$ ), along with a band at  $1220\text{ cm}^{-1}$ , due to the bending mode of  $\text{CH}_2\text{—S}$ , confirmed that CdTe was on the APS/ZnO400 surface.

The amount of  $-\text{NH}_3^+$  groups anchored on the ZnO400 surface was estimated by thermogravimetric analysis. The TGA profile of the APS/ZnO400 sample is reported in Figure 8B (curve b) and compared with that of pure ZnO400 (Figure 8B, curve a). Besides a weight loss at low temperatures, due to the presence of adsorbed water, the TGA profile of the APS/ZnO400 sample showed an additional weight loss in the  $200\text{--}500\text{ °C}$  range assigned to the thermal decomposition of the protonated aminopropyl groups. The amount of ammonium groups anchored on the ZnO400 surface was estimated to be ca. 3 wt %.

Particular attention was finally devoted to the investigation of the optical properties of the ZnO nanosheets before and after functionalization with  $-\text{NH}_3^+$  groups and CdTe nanocrystals.

DR-UV-vis spectra of ZnO400, APS/ZnO400, and CdTe/ZnO400 samples are reported in Figure 9A. Prior to the analysis, ZnO400 and APS/ZnO400 were treated in vacuum at  $150\text{ °C}$  for 1 h to remove the adsorbed water, while the CdTe/ZnO400 sample was heated in vacuum at low temperatures (ca.  $50\text{ °C}$ ) to avoid CdTe decomposition and to preserve the photophysical properties of the nanocrystals.



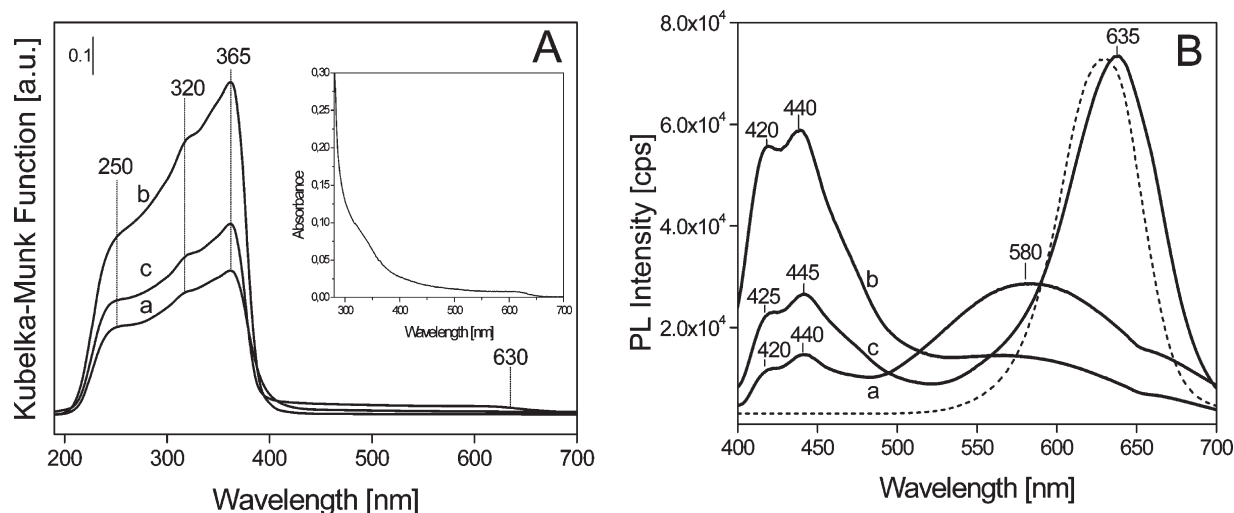


**Figure 9.** DR-UV-vis spectra (A) of the ZnO400 (a), APS/ZnO400 (b), and CdTe/ZnO400 (c) samples recorded in vacuum; UV-vis spectrum of CdTe in water suspension is reported in the inset. (B) Photoluminescence spectra of the samples ZnO400 (a), APS/ZnO400 (b), and CdTe/ZnO400 (c) and pure CdTe nanocrystals in water suspension (short dash line), collected by an excitation wavelength of 370 nm.

As a general feature, the DR-UV-vis spectra of all samples showed three bands at 365, 320, and 250 nm. The absorption at 365 nm is generally assigned to the electronic transition from the valence band (mainly formed by orbitals of the oxide anions) to the conduction band (mainly formed by orbitals of the  $\text{Zn}^{2+}$  cations) of ZnO.<sup>33,34</sup> The band gap estimated for this transition was 3.30 eV, and this value is in good agreement with the band gap typical of bulky ZnO samples (3.37 eV).

The bands at lower wavelengths can be due to the structure of the conductive electronic band of ZnO occurring when the particle sizes of the semiconductive material are below 20 nm.

Besides the absorptions typical of the ZnO matrix, the DR-UV-vis spectrum of the CdTe/ZnO400 (Figure 9, c) showed an additional absorption at 630 nm typical of CdTe nanocrystals (see inset in Figure 9A), thus confirming their presence on the ZnO surface.

Photoluminescence spectra of ZnO400, APS/ZnO400, and CdTe/ZnO400 are reported in Figure 9B. The ZnO400 sample (Figure 9B, a) showed two weak emissions at 420 and 440 nm and an intense and wide band centered at ca. 580 nm. The emissions at low wavelengths were assigned to the radiative decay from the conductive to the valence band of ZnO,<sup>35</sup> whereas the band at 580 nm could be assigned to surface defects.<sup>36</sup> The latter band was in fact largely quenched after the anchoring of silane species, as a consequence of the modification of the surface properties of the support, thus confirming that ZnO surface defects are highly efficient emitting centers (Figure 9B, b).

The emission spectrum of CdTe/ZnO400 (Figure 9B, c) was dominated by an intense band at 635 nm, typical of CdTe nanocrystals, thus indicating that the presence of luminescent nanoentities allowed us to modulate the emission properties of ZnO nanosheets.

In conclusion, this work presented a simple and effective route for the preparation of ZnO-based nanostructured materials with a fine-tuning emission because specific emitting nanoentities (i.e., CdTe with variable particle size) can be easily anchored on the surface of functionalized ZnO nanosheets. The combination of different quantum dots with specific optical properties with a semiconductive inorganic support could allow the development

of light-emitting devices with high quantum efficiency and good performances.

## CONCLUSIONS

ZnO nanosheets were obtained through the decomposition of the  $\text{Zn}_4\text{CO}_3(\text{OH})_6 \cdot \text{H}_2\text{O}$  precursor at increasing temperatures (i.e., 300, 400, and 500 °C), and XRD studies indicated that their crystallinity was strongly dependent on the calcination temperature. The ZnO sample prepared by precursor calcination at 500 °C showed the highest crystallinity.

SEM and TEM microscopy data suggested that the increase of the calcination temperature was associated with the diminishing of the size of ZnO nanosheets that are also arranged in a more regular fashion. This has a positive effect on the conductive properties of the solids that are significantly improved by increasing the calcination temperature. The solid prepared by decomposing the precursor at 300 °C showed an insulating behavior, whereas the ZnO materials prepared at higher temperature were characterized by  $I/V$  curves typical of semiconductors.

Interestingly, due to the progressive reduction of the intraparticle porosities by increasing the decomposition temperature (as estimated by TEM and a nitrogen adsorption isotherm at -196 °C), the specific surface area of the ZnO solids was found to decrease passing from 68 m<sup>2</sup>/g for ZnO300 to 25 m<sup>2</sup>/g for ZnO500.

The collected data allowed us to select the most suitable solid to be used as a host for the introduction of luminescent CdTe NCs by silylating the ZnO surface with aminopropylsilane and then using the  $\text{NH}_3^+$  groups to promote ionic interactions with negatively charged NCs. The ZnO400 sample was selected as the host solid due to its physicochemical properties, ensuring a good electrical conductivity, together with an adequate amount of surface OH groups suitable for silylation reaction.

This modification was successfully conducted in acid conditions, and the obtained APS/ZnO400 sample contained ca. 3% of organic species.

CdTe NCs were successfully confined on the solid surface, as suggested by HRTEM and FTIR spectroscopy.

The functionalization of the ZnO surface with luminescent NCs allowed us to modify the emission properties of the final solid, rendering this hybrid material a good candidate for the development of new optoelectronic devices.

## ■ ASSOCIATED CONTENT

**S Supporting Information.** Additional information on the physicochemical characterization of the final hybrid material. This material is available free of charge via the Internet at <http://pubs.acs.org>.

## ■ AUTHOR INFORMATION

### Corresponding Author

\*Fax: +39 0131 360250. Tel: +39 0131 360216. E-mail: chiara.bisio@mf.unicmn.it.

## ■ ACKNOWLEDGMENT

The financial support of Regione Piemonte (CIPE 2006 Project, “Novel Nanostructured Materials for Light Emitting Devices and Application to Automotive Displays”) and of European research Project “INNOVASOL”, No. FP7-ENERGY-NMP-2008-1 “Innovative Materials for Future Generation Excitonic Solar Cells” is gratefully acknowledged. The authors acknowledge Prof. A. Eychmueller and Dr. V. Lesnyak (Technische Universität Dresden) for CdTe NCs supply and Dr. Luca Bertinetti and Ms. Federica Franconieri (University of Turin) for TEM measurements.

## ■ REFERENCES

- (1) Fu, Y.-S.; Du, X.-W.; Kulinich, S. A.; Qiu, J.-S.; Qin, W.-J.; Li, R.; Sun, J.; Liu, J. *J. Am. Chem. Soc.* **2007**, *129*, 16029–16033.
- (2) Zhang, Q.; Chou, T. P.; Russo, B.; Jenekhe, S. A.; Cao, G. *Angew. Chem., Int. Ed.* **2008**, *47*, 2402–2406.
- (3) Baxter, J. B.; Walker, A. M.; van Ommering, K.; Aydil, E. S. *Nanotechnology* **2006**, *17*, S304–S312.
- (4) Li, C. C.; Du, Z. F.; Li, L. M.; Yu, H. C.; Wan, Q.; Wang, T. H. *Appl. Phys. Lett.* **2007**, *91*, 032101–032103.
- (5) Zhou, J.; Fei, P.; Gao, Y.; Gu, Y.; Liu, J.; Bao, G.; Wang, Z. L. *Nano Lett.* **2008**, *8*, 2725–2729.
- (6) Tam, K. H.; Djurišić, A. B.; Chan, C. M. N.; Xi, Y. Y.; Tse, C. W.; Leung, Y. H.; Chan, W. K.; Leung, F. C. C.; Au, D. W. T. *Thin Solid Films* **2008**, *516*, 6167–6174.
- (7) Tang, Q.; Li, Y.; Zhou, Z.; Chen, Y.; Chen, Z. *ACS Appl. Mater. Interfaces* **2010**, *2* (8), 2442–2447.
- (8) Solnyshkov, D. D.; Weiss, T.; Malpuech, G.; Gippius, N. A. *Appl. Phys. Lett.* **2011**, *99* (11), 111110.
- (9) Liu, C.; Zapien, J. A.; Yao, Y.; Meng, X.; Lee, C. S.; Fan, S.; Lifshitz, Y.; Lee, S. T. *Adv. Mater.* **2003**, *15*, 838–841.
- (10) Dorfman, A.; Kumar, N.; Hahn, J. *Langmuir* **2006**, *22*, 4890–4895.
- (11) Dorfman, A.; Kumar, N.; Hahn, J. *Adv. Mater.* **2006**, *18*, 2685–2690.
- (12) Qiu, J.; Guo, M.; Wang, X. *ACS Appl. Mater. Interfaces* **2011**, *3* (7), 2358–2367.
- (13) Bai, X. D.; Gao, P. X.; Wang, Z. L. *Appl. Phys. Lett.* **2003**, *82*, 4806–4808.
- (14) Tseng, Y. K.; Hsu, H. C.; Hsieh, W. F.; Liu, K. S.; Chen, I. C. *J. Mater. Res.* **2003**, *18*, 2837–2844.
- (15) Pan, Z. W.; Dai, Z. R.; Wang, Z. L. *Science* **2001**, *291*, 1947–1949.
- (16) Umar, A.; Hahn, Y. B. *Nanotechnology* **2006**, *17*, 2174–2180.
- (17) Umar, A.; Lee, S.; Im, Y. H.; Hahn, Y. B. *Nanotechnology* **2005**, *16*, 2462–2468.
- (18) Wei, A.; Sun, X. W.; Xu, C. X.; Dong, Z. L.; Yu, M. B.; Huang, W. *Appl. Phys. Lett.* **2006**, *88*, 213102–213105.
- (19) Cao, B.; Cai, W.; Zeng, H.; Duan, G. *J. Appl. Phys.* **2006**, *99*, 073516–073521.
- (20) Xu, L.; Guo, Y.; Liao, Q.; Zhang, J.; Xu, D. *J. Phys. Chem. B* **2005**, *109*, 13519–13522.
- (21) Le, H. Q.; Chua, S. J.; Koh, Y. W.; Loh, K. P.; Fitzgerald, E. A. *J. Cryst. Growth* **2006**, *293*, 36–42.
- (22) Liu, C.; Masuda, Y.; Wu, Y.; Takai, O. *Thin Solid Films* **2006**, *503*, 110–114.
- (23) Wang, J.; Tsuzuki, T.; Sun, L.; Wang, X. *ACS Appl. Mater. Interfaces* **2010**, *2* (4), 957–960.
- (24) Xu, C. H.; Lui, H. F.; Surya, C. *Mater. Lett.* **2011**, *65* (1), 27–30.
- (25) Govender, K.; Boyle, D. S.; Kenway, P. B.; O’Brien, P. *J. Mater. Chem.* **2004**, *14*, 2575–2591.
- (26) Lee, J.-Y.; Yin, D.; Horiuchi, S. *Chem. Mater.* **2005**, *17*, 5498–5503.
- (27) Peng, W.; Qu, S.; Cong, G.; Wang, Z. *Cryst. Growth Des.* **2006**, *6*, 1518–1522.
- (28) Bai, W.; Zhu, X.; Zhu, Z.; Chu, J. *Appl. Surf. Sci.* **2008**, *254*, 6483–6488.
- (29) Bera, A.; Basak, D. *ACS Appl. Mater. Interfaces* **2010**, *2* (2), 408–412.
- (30) Song, Y.; Cao, X.; Guo, Y.; Chen, P.; Zhao, Q.; Shen, G. *Chem. Mater.* **2009**, *21*, 68–77.
- (31) Kakiuchi, K.; Hosono, E.; Kimura, T.; Imai, H.; Fujihara, S. *J. Sol-Gel Sci. Technol.* **2006**, *39*, 63–72.
- (32) Borisov, Y. A.; Papkov, V. S.; Rabkina, A. Y.; Zavin, B. G. *J. Mol. Struct. (Theochem)* **2003**, *664–665*, 157–170.
- (33) Sakthivel, S.; Geissen, S. U.; Bahnemann, D. W.; Murugesan, V.; Vogelpohl, A. *J. Photochem. Photobiol. A* **2002**, *148*, 283–293.
- (34) Bordiga, S.; Lamberti, C.; Ricchiardi, G.; Regli, L.; Bonino, F.; Damin, A.; Lillerud, K.-P.; Bjorgen, M.; Zecchina, A. *Chem. Commun.* **2004**, 2300–2301.
- (35) Patra, M. K.; Manoth, M.; Singh, V. K.; Siddaramana Gowd, G.; Choudhry, V. S.; Madera, S. R.; Kumar, N. *J. Lumin.* **2009**, *129*, 320–324.
- (36) Fan, X. M.; Lian, J. S.; Guo, Z. X.; Lu, H. J. *Appl. Surf. Sci.* **2005**, *239*, 176–181.